



# Continuous monitoring of forest disturbance using all available Landsat imagery

Zhe Zhu\*, Curtis E. Woodcock, Pontus Olofsson

Center for Remote Sensing, Department of Geography and Environment, Boston University, 675 Commonwealth Avenue, Boston, MA 02215, USA

## ARTICLE INFO

Available online 17 February 2012

### Keywords:

Continuous monitoring  
Forest disturbance  
CMFDA  
Change detection  
Landsat

## ABSTRACT

A new change detection algorithm for continuous monitoring of forest disturbance at high temporal frequency is developed. Using all available Landsat 7 images in two years, time series models consisting of sines and cosines are estimated for each pixel for each spectral band. Dropping the coefficients that capture inter-annual change, time series models can predict surface reflectance for pixels at any location and any date assuming persistence of land cover. The Continuous Monitoring of Forest Disturbance Algorithm (CMFDA) flags forest disturbance by differencing the predicted and observed Landsat images. Two algorithms (single-date and multi-date differencing) were tested for detecting forest disturbance at a Savannah River site. The map derived from the multi-date differencing algorithm was chosen as the final CMFDA result, due to its higher spatial and temporal accuracies. It determines a disturbance pixel by the number of times “change” is observed consecutively. Pixels showing “change” for one or two times are flagged as “probable change”. If the pixel is flagged for the third time, the pixel is determined to have changed. The accuracy assessment shows that CMFDA results were accurate for detecting forest disturbance, with both producer's and user's accuracies higher than 95% in the spatial domain and temporal accuracy of approximately 94%.

© 2012 Elsevier Inc. All rights reserved.

## 1. Introduction

The 39 years of data in the Landsat archive comprise the most valuable dataset available for understanding land cover change, such as deforestation, urban growth, agriculture expansion, and wetland loss (Coiner, 1980; Coppin & Bauer, 1994; Cohen et al., 1998; Jensen et al., 1995; Masek et al., 2008; Seto et al., 2002). Due to the large amount of carbon stored in forests, monitoring forest change is of great importance for understanding the global carbon budget. Knowing where and when forest disturbance happens is crucial for forest management and carbon cycle modeling. Numerous forest change detection algorithms have been developed, validated, and applied to different parts of the world (see for example Collins & Woodcock, 1996; García-Haro et al., 2001; Goodwin et al., 2008; Hayes & Sader, 2001; Healey et al., 2005; Healey et al., 2006; Hilker et al., 2009; Hostert et al., 2003; Huang et al., 2010; Kennedy et al., 2007; Kennedy et al., 2010; Masek et al., 2008; Vogelmann et al., 2009; Woodcock et al., 2001).

Most of the change detection algorithms are based on two dates of Landsat images (see for example Collins & Woodcock, 1996; Healey et al., 2005; Healey et al., 2006; Masek et al., 2008; Woodcock et al., 2001). These algorithms are simple to use, but not always applicable. One problem is that both images have to be at the same time of year to minimize phenology differences and Bidirectional Reflectance Distribution Function (BRDF) effects. The other problem is that the input

images need to be cloud and snow free. Even under these conditions, these change detection algorithms can only provide the spatial pattern of the disturbance that occurred between the two images and it is impossible to know when the change occurred in the time between the two images. This is important because the time period between images is frequently as much as five or ten years.

Based on the idea that forest change can be better detected using many observations of a place and the increasing need for detecting changes as they are occurring, a number of methods for change detection using many dates of Landsat imagery have been developed (Goodwin et al., 2008; Hilker et al., 2009; Hostert et al., 2003; Huang et al., 2010; Kennedy et al., 2007; Kennedy et al., 2010; Vogelmann et al., 2009). These algorithms have been shown to be more automatic in identifying forest change and more robust to noise from registration, BRDF, and seasonal effects.

Nevertheless, these newly developed algorithms still have limitations in image selection, as all the images used should be within the growing season to minimize phenology and BRDF differences and at the same time they should be almost cloud and snow free to make multi-temporal image differencing possible. Though some new indices such as the Integrated Forest Z-score (IFZ) (Huang et al., 2010) and Disturbance Index (DI) (Healey et al., 2005; Healey et al., 2006; Masek et al., 2008) can reduce phenology and BRDF effects by normalizing the indices with a predefined forest sample, they may have problems when handling data from different seasons or within heterogeneous areas where both deciduous and evergreen forests exist. Therefore, cloud and snow free Landsat images from three of the seasons will not be able to be used. Sometimes images acquired during times other than the growing

\* Corresponding author. Tel.: +1 617 233 6031.

E-mail address: [zhuzhe@bu.edu](mailto:zhuzhe@bu.edu) (Z. Zhu).

season, such as winter images, can be more useful than growing season images for detecting subtle disturbance (pest infestation) when the forest understories are dense during the growing season, which makes the mixed signal almost the same as healthy forest (Bolton & Woodcock, *in preparation*). Some studies even found that snow-covered Landsat imagery can be used for change detection, often allowing for a longer period of observed changes than the growing season (Takao, 2003). Due to the requirement for cloud and snow free images acquired during the growing season, most of the multi-temporal change detection algorithms can only provide annual or biennial change results.

Recently, Hilker et al. (2009) used both Moderate Resolution Imaging Spectroradiometer (MODIS) and Landsat to detect forest disturbance in Canada. By blending MODIS and Landsat data, a high temporal frequency (16 days) and fine spatial resolution (30 m) disturbance map was produced. Though this algorithm can identify the time of forest disturbance at a high frequency, it may take a long time to acquire two clear Landsat images for MODIS and Landsat data blending. If we want to monitor immediate problems such as illegal logging or encroachment on protected area, we need an algorithm that can monitor changes as they are occurring (within a few weeks) and can update the change results as soon as a new observation is available.

Because of the limitations of existing algorithms for fully tapping the Landsat archive, we developed the Continuous Monitoring of Forest Disturbance Algorithm (CMFDA), which uses all available Landsat images to characterize forest disturbance. CMFDA considers each pixel separately, taking advantage of any clear views for each pixel to track spectral trends over time. In this study we are only focusing on human-induced forest disturbance (forest clear-cut/thinning), though CMFDA may be able to identify other natural-induced forest disturbances that cause surface reflectance to deviate from expected values. CMFDA produces a map showing where and when the disturbance happens at high spatial resolution (30 m) and temporal frequency (a few weeks). Currently, the highest temporal frequency for CMFDA is 8 days when both Landsat 5 and Landsat 7 are used. Clouds and cloud shadows are flagged as part of the procedure. The following steps are necessary to implement and test CMFDA:

1. A two-step cloud, cloud shadow, and snow masking approach.
2. Estimate time series models of surface reflectance.
3. Define a stable forest mask
4. Predict the “next” clear observations to serve as a basis for comparison with new observations.
5. Detect forest disturbance with the single-date and multi-date differencing algorithms
6. Test the disturbance map derived from the algorithms against an independently-derived reference map.

## 2. Study area and data

The study area (Fig. 1) is located in the Savannah River Basin covering 2000 × 2000 Landsat pixels (60 × 60 km). The Savannah River is along the border between Georgia and South Carolina. There is a variety of land covers in this study area. Along the Savannah River, there is a large area of deciduous forest and wetland. Most of this study area is covered by evergreen forest and agriculture. Three urban areas (Sylvania, Allendale, and Estill) along the Savannah River are within the study area. Though there is no snow present in this study area, it is frequently cloudy. By applying a newly developed cloud and cloud shadow detection algorithm called Fmask (Function of mask) (Zhu & Woodcock, 2012) to all available Landsat ETM+ images (Path 17 and Row 37) from 2001 to 2002 (Fig. 2), the expected frequency of cloudy observations for each pixel was approximately 50% and almost all the cloud free images were acquired at the beginning or end of the year (Fig. 3). The cloud cover during the growing season was always heavy. There was not a single cloud free ETM+ image during the growing season for either 2001 or 2002.

We used a time series of Landsat Thematic Mapper (TM) and Enhanced Thematic Mapper Plus (ETM+) images for Path 17 and Row 37. All available ETM+ L1T images (a total of 64) acquired from 2001 to 2004 were downloaded if the cloud cover was less than 90%. Because the year 2003 was the time that CMFDA was applied to find disturbances and also the year when Scan Line Corrector failed in Landsat 7, all available TM L1T images (a total of 12) acquired in 2003 were downloaded if cloud cover was less than 90% to help find the disturbance time with higher frequency.

## 3. Methods

CMFDA has many component parts, including: image preprocessing; single-date masking of clouds, cloud shadows, and snow; multi-temporal masking of clouds, cloud shadows, and snow; estimation of surface reflectance models; mapping of stable forest; predicting the “next” Landsat observations, and identification of forest disturbance (Fig. 4).

### 3.1. Preprocessing

Geometric registration and radiometric normalization are important steps in change detection, facilitating comparison of change indices across time and space. We assume Landsat L1T images are already precisely registered and sub-pixel misregistration will not influence our analysis. All the Landsat images were atmospheric corrected with the Landsat Ecosystem Disturbance Adaptive Processing System (LEDAPS), using the 6S radiative transfer approach (Masek et al., 2006; Vermote et al., 1997).

### 3.2. Cloud, cloud shadow, and snow masking

Clouds, cloud shadows, and snow are noise in the data and their detection is the first step in the analysis (Arvidson et al., 2001; Irish, 2000; Simpson & Stitt, 1998). The brightening effect of clouds or snow and the darkening effect of cloud shadows can be confused with land cover change if they are not screened. Historically, estimates of cloud cover in Landsat data have been provided by the Automatic Cloud Cover Assessment (ACCA) system (Irish, 2000; Irish et al., 2006). It works well for estimating the overall percentage of clouds in each Landsat scene. However, it does not provide sufficiently precise location and boundaries of clouds and their shadows to support automated analysis of a time series of Landsat data to find change.

A two-step cloud, cloud shadow, and snow masking algorithm has been developed that provides the levels of accuracy we need. The first step (Fmask) uses a newly developed algorithm that processes each Landsat scene individually. The second step builds on the results of the first step and identifies cloud, cloud shadow and snow based on a time series of Top Of Atmosphere (TOA) reflectances of each pixel (Zhu et al., *in preparation*). Though the first step is a significant improvement over ACCA, it is not perfect, as it applies the same scene-based probability threshold for all the pixels in the scene. The second step further improves the cloud, cloud shadow, and snow masking using the additional temporal information. Since the first step can screen most of the cloud, cloud shadow, and snow pixels, in the second step, a model consisting of sines and cosines is fit for each pixel using all remaining clear observations. The Robust Iteratively Reweighted Least Squares (RIRLS) method is applied to reduce the influence of outliers during the fitting (DuMouchel & O'Brien, 1989; Holland & Welsch, 1977; O'Leary, 1990; Street et al., 1988). The outliers (missed clouds, cloud shadows, and snow) are easily recognized by comparing the actual observations and the model predicted values.

The two-step cloud masking results are illustrated in Fig. 5. The image on the left is the original Landsat image. The images in the center and on the right show the semi-transparent cloud/cloud shadow masks overlaid on the original image. We dilate the clouds and



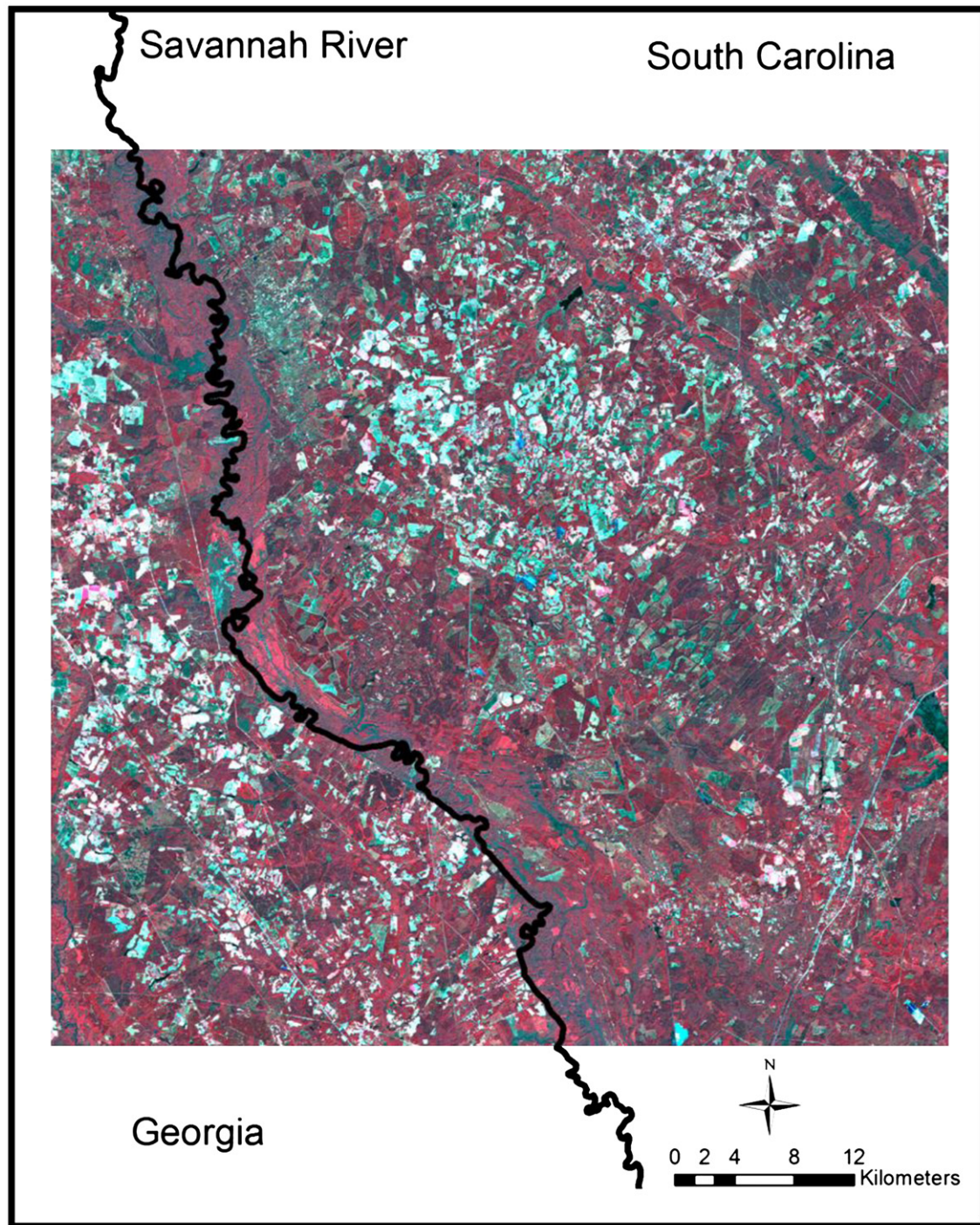
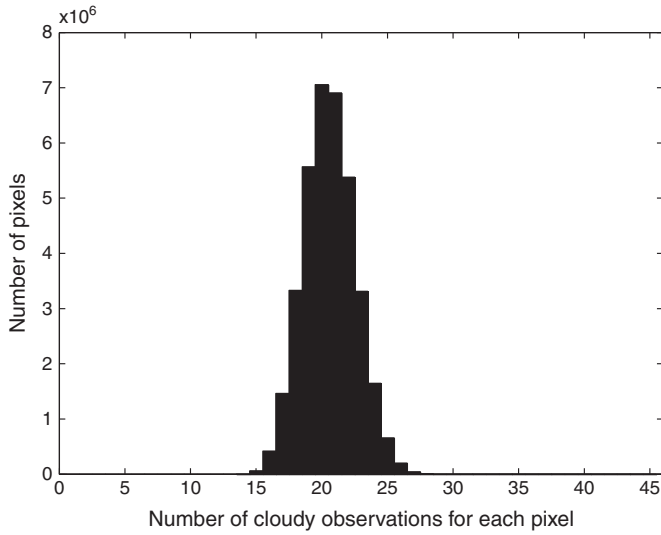


Fig. 1. Study area (subset of November 23 rd 2002 Landsat ETM+ image shown with Bands 4, 3, and 2 in red, green, and blue).

shadows by 3 pixels in an attempt to exclude the edges of clouds and shadows that are often spectrally inseparable from the rest of the image. Fmask (Fig. 5b) misses a few clouds and cloud shadows (yellow arrows). If we examine the time series of clear observations for two deciduous forest pixels indicated by the yellow arrows, the missed cloud and cloud shadow pixels would bias a model fit using Ordinary Least Square (OLS) (green circles), but have little influence on the RIRLS method (red cycles) (Fig. 6). With the help of the predicted values, the missed cloud and cloud shadow pixels were easily detected in the second step (Fig. 5c).

### 3.3. Estimating the surface reflectance model

After removing observations covered by clouds, cloud shadows, and snow, CMFDA uses the remaining clear Landsat observations to estimate surface reflectance models for each pixel based on OLS fitting. At this stage, OLS fitting is used rather than RIRLS simply because it is faster and any significant outliers have been removed. The surface reflectance model is a function of sines and cosines shown in Eq. (1). It includes a two term harmonic (Fourier) model (Davis, 1986; Rayner, 1971) and an inter-annual change model newly developed



**Fig. 2.** Histogram showing the frequency of cloudy observations from 2001 to 2002 for all available ETM+ images. There were 46 images from this time period, indicating that about half of all observations collected were cloudy. Notice that this is not the same as saying half the images were cloud free.

here. The two term harmonic model ( $i = 1$  and  $N + 1$ ) is used to capture the seasonality and BRDF effects of the annual surface reflectance. The harmonic model is chosen due to the advantage of requiring fewer coefficients to estimate (fewer necessary clear observations) and being less sensitive to short term data variations and inherent noise (e. g., missed clouds, cloud shadows, snow, and image misregistration). The inter-annual change model ( $i = 2, 3, 4 \dots N$ ) is comprised of sines and cosines that represent variation that occur on an  $i$ -year cycle, which mostly result from land cover change:

$$f(x) = a_0 + \sum_{i=1}^N \left( a_i \cos\left(\frac{2\pi}{iT}x\right) + b_i \sin\left(\frac{2\pi}{iT}x\right) \right) + a_{N+1} \cos\left(\frac{2\pi}{0.5T}x\right) + b_{N+1} \sin\left(\frac{2\pi}{0.5T}x\right) \quad (1)$$

where,

- $x$  Day-of-year.
- $N$  Number of years.
- $T$  Number of days per year ( $T = 365$ ).
- $a_0$  Coefficient represents overall surface reflectance.
- $a_i, b_i$  Coefficients that capture the changes of surface reflectance for the  $i^{\text{th}}$  year.
- $a_{N+1}, b_{N+1}$  Coefficients that capture the bimodal variations of surface reflectance for each year.

Two years (2001 and 2002) of Landsat ETM+ images (33 images) were used to estimate the surface reflectance model for the Savannah River site. In this case, there are 7 parameters for each surface reflectance model. The last two parameters  $a_3$  and  $b_3$  are used to capture the bimodal variations for each year, which mostly occurs in agricultural areas due to an initial period of growth in the spring that is followed by plowing and a second period of growth. The parameters  $a_1$  and  $b_1$  are used to capture the annual change caused by phenology and BRDF effects. The inter-annual change is captured by the two parameters  $a_2$  and  $b_2$ . The mean overall surface reflectance for the two years is represented by  $a_0$ . To estimate these 7 parameters, at least 7 clear observations are necessary in two years. To strengthen the robustness of the fitting, CMFDA only estimates a pixel if the number of clear observation is more than one and a half times of the number of total parameters to be estimated, that is a total of 11 clear observations. Considering the 23 observations per year from Landsat 7 and 23 observations per year from Landsat 5 per year at this U.S. site, 11 clear observations in two years are easily obtained even though there were very few cloud free images. In fact, when only using the ETM+ images, the highest number of cloudy observations at the pixel level is 28 (Fig. 2), meaning there would be at least 18 clear observations for each pixel between 2001 and 2002.

### 3.4. Defining a stable forest mask

Some land uses exhibit abrupt changes in surface reflectance that do not represent land use change. For example, agricultural fields are plowed, resulting in reflectance changes that do not represent land use change. To limit our change detection efforts to forests, we

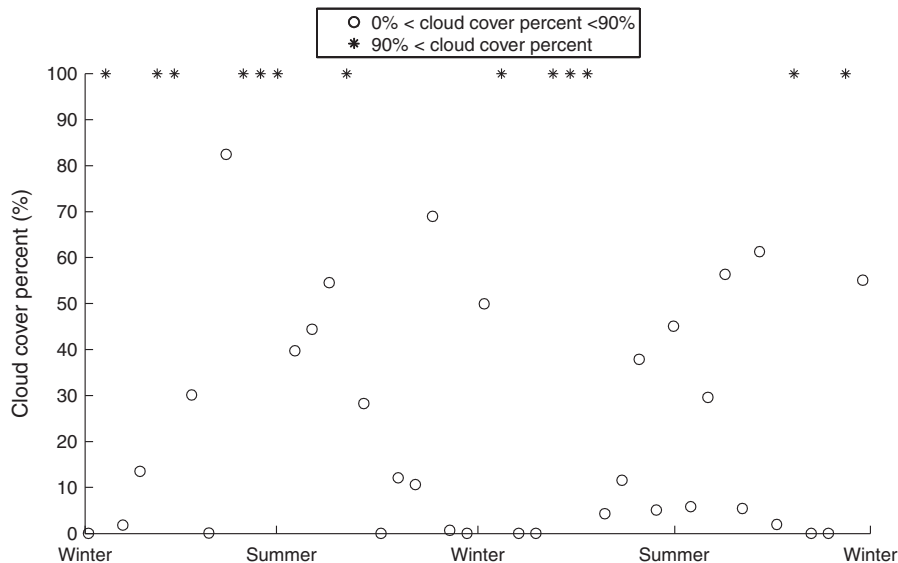


**Fig. 3.** Cloud cover percent of all available ETM+ images from 2001 to 2002. Notice that during the peak growing season (summer), not a single ETM+ image was “cloud free” (meaning zero percent cloud cover).



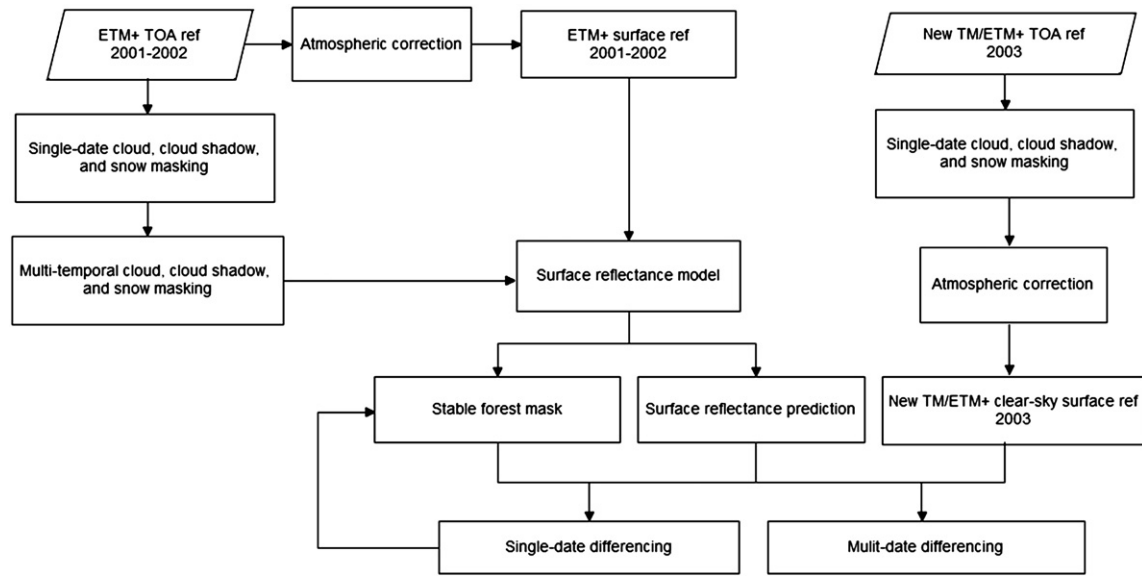


Fig. 4. Flow chart of Continuous Monitoring of Forest Disturbance Algorithm.

created a stable forest mask and only assessed these pixels for change. The stable forest mask was produced automatically using the estimated coefficients derived from the 33 Landsat ETM+ images acquired between 2001 and 2002 based on the fact that forests are observed to have high NDVI values (Masek et al., 2008) and low reflectance in the SWIR bands (Huang et al., 2010; Kennedy et al., 2007). As compared to Band 5, Band 7 is more robust to different atmosphere conditions, so we chose Band 7 as our SWIR band for extracting forests. From the previous surface reflectance models we have the overall surface reflectance represented by  $a_{0,i}$  ( $i=1, 2, 3, 4, 5$ , and  $7$ ), where  $i$  stands for the Landsat TM or ETM+ band number. Therefore, the overall NDVI values can be calculated with Band 4 and Band 3 overall surface reflectance model coefficients ( $a_{0,3}$  and  $a_{0,4}$ ) and the overall Band 7 surface reflectance ( $a_{0,7}$ ). We define a possible forest

pixel if it meets the criteria that overall NDVI is larger than 0.6 and overall Band 7 reflectance is less than 0.1. To better illustrate how the two thresholds work, we plotted ten samples of the time series for each land cover class for Band 7 and NDVI (Fig. 7). In Fig. 7, the overall forest NDVI values are always above 0.6, but sometimes other vegetation types like crop, grass, and shrub can also have overall forest NDVI values above 0.6. As forests are usually dark in SWIR bands compared to other vegetation types, a threshold of 0.1 in overall Band 7 surface reflectance excludes other vegetation types that may have high NDVI values.

If land cover change occurs within the estimating period (2001–2002), future use of the resulting model will be problematic. Therefore, we excluded these pixels that were changed during the estimating period from the stable forest mask. As parameters  $a_2$  and  $b_2$

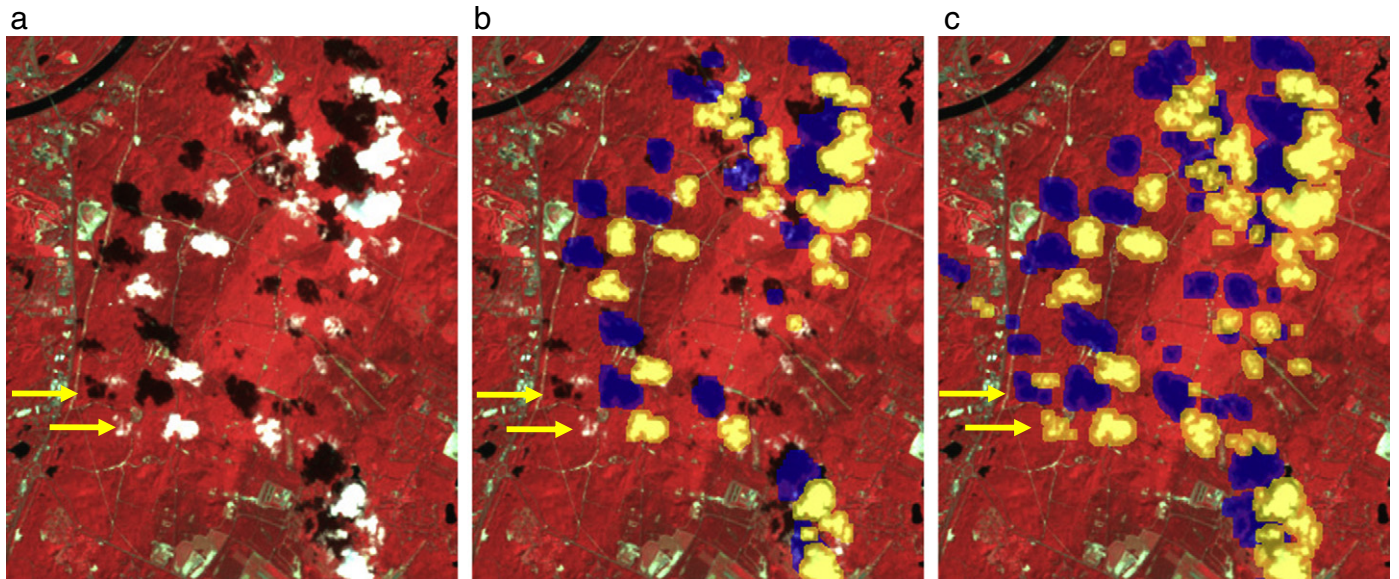
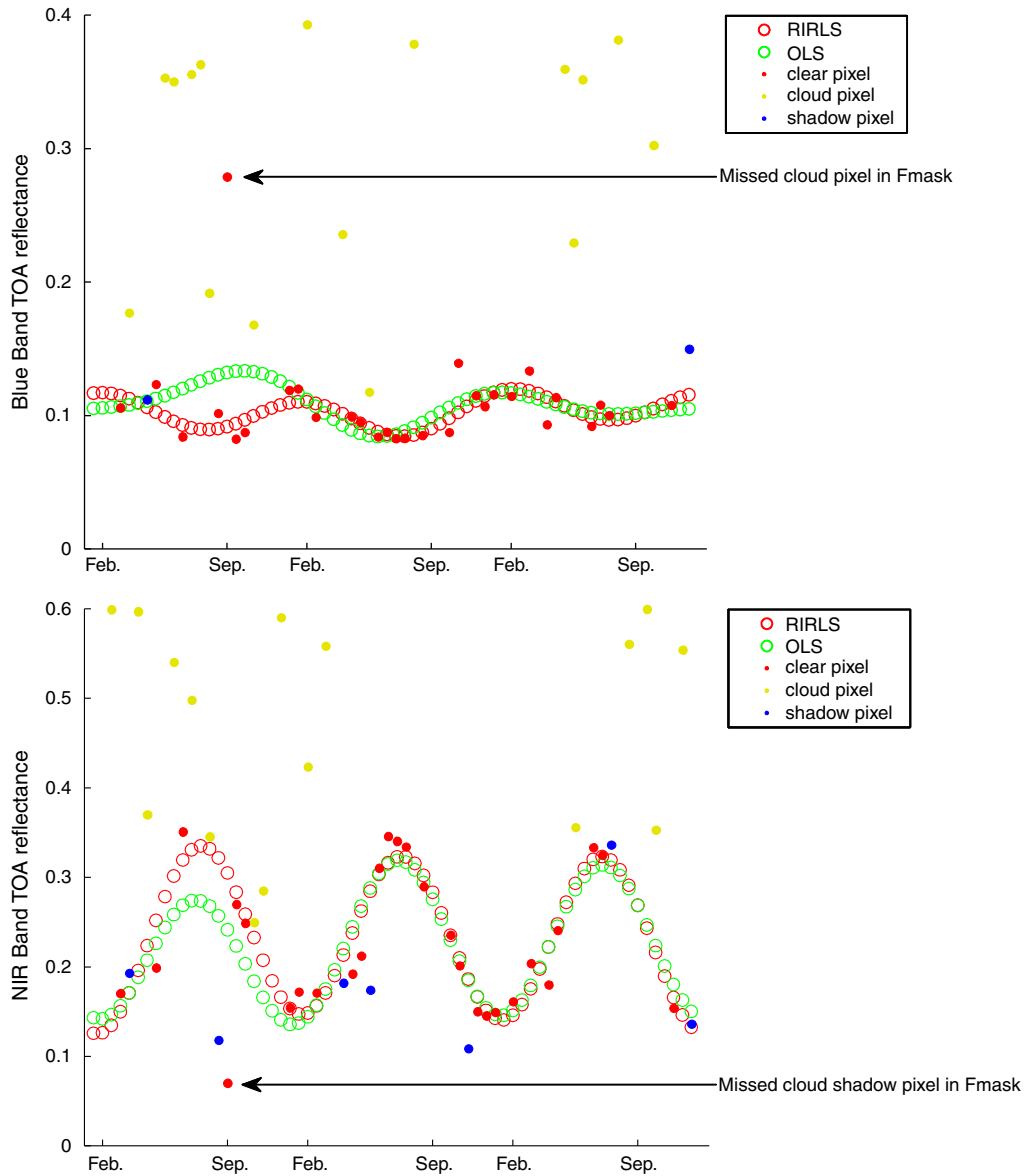


Fig. 5. Illustration of the two-step cloud, cloud shadow, and snow masking results. Fig. 5a shows a small piece of a Landsat image (shown with Bands 4, 3, and 2 in red, green, and blue). Fig. 5b shows the results of the Fmask algorithm. Clouds are yellow and shadows are blue. Fig. 5c shows the results after use of the multi-temporal approach. Notice that the cloud and cloud shadow missed in Fig. 5b were found in Fig. 5c.



**Fig. 6.** (top) and (bottom) show a 3 year time series of Landsat Band 1 and Band 4 TOA reflectance for two deciduous forest pixels. Fmask divided observations into three groups: cloud (yellow), shadow (blue), and clear (red). Notice that when viewed in the context of the timeseries, cloudy or shadowed observations that were within the thresholds of Fmask became easy to identify. There are two time series models shown in each of the figures. The green circles show the result of an OLS fit to the time points without removing the missed cloud (or shadow). Notice that the missed cloud or shadow has a significant effect on the time series result in this case. The green circles show the result of fitting the time series model using the RIRLS method, which minimized the effect of outliers. Note that in this case the result is not adversely affected by the missed cloud (or shadow).

capture the inter-annual differences, their amplitude represents the degree of changes (excluding phenology and BRDF differences) in surface reflectance within the estimating period. In this study, surface reflectance parameters computed from Band 7 were used for detecting changes that occurred in the estimating period because of their robustness to atmospheric influences and sensibility to forest disturbance. A threshold for pixels where  $\sqrt{a_{2,7}^2 + b_{2,7}^2}$  is larger than 0.02 worked well in identifying the pixels that changed during the estimating period. However, if change occurs at the end of the estimating period, one or two changed observations may not contribute enough to the inter-annual change parameters, making  $\sqrt{a_{2,7}^2 + b_{2,7}^2}$  still less than 0.02.

As the model cannot capture forest disturbance that happened at the end of the estimating period, the predicted values from the model will still have similar values as if no change occurred. In this case, these disturbed pixels can be easily identified by comparing

the last clear observations with the predicted values (see Section 4.1.1 for detail). The final stable forest map is created by combining all these criteria above in Eq. (2) and the final stable forest mask is shown in Fig. 8.

$$\text{Stable forest mask} = \frac{a_{0,4} - a_{0,3}}{a_{0,4} - a_{0,3}} > 0.6 \text{ and } a_{0,7} < 0.1 \text{ and } \sqrt{a_{2,7}^2 + b_{2,7}^2} < 0.02$$

(2)

The use of the magnitude of the interannual change parameters ( $a_2$  and  $b_2$ ) to find change represents a new kind of method for finding change retrospectively. Since we are pursuing methods for monitoring forest change as it is occurring, we used this approach here only to find changes during the estimating period so that they won't be confused with forest change in the testing period.

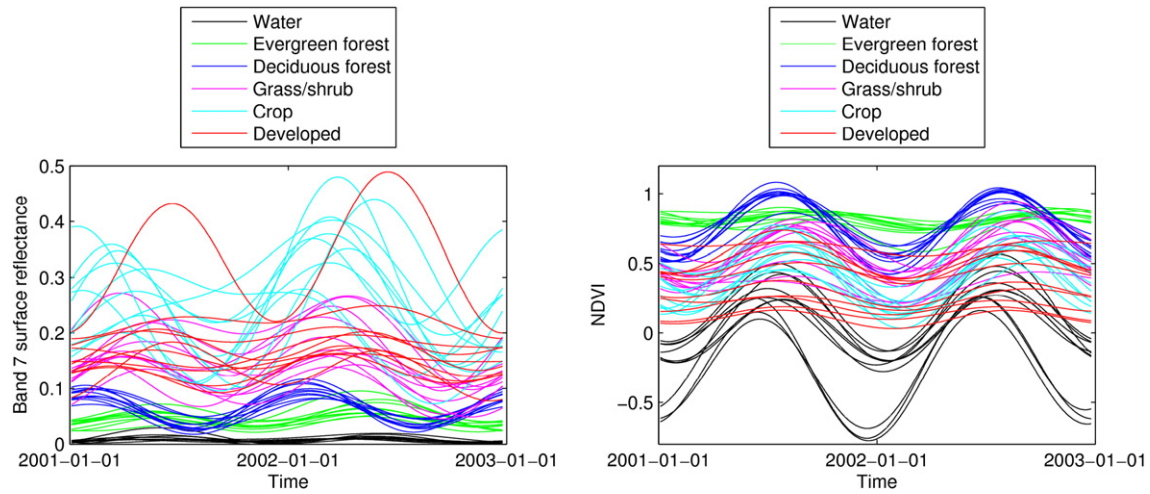


**Fig. 7.** Estimated Band 7 and NDVI temporal trajectories of different land cover classes between 2001 and 2002. For each land cover class, ten time series of samples were estimated for their surface reflectance models.

### 3.5. Predicting the “next” Landsat image

Assuming no land cover change has occurred, Eq. (3) is used to predict the surface reflectance for each pixel and each spectral band at any time of the year, or the equivalent of the “next” Landsat image. The parameters were previously estimated using Eq. (1) based on images between 2001 and 2002. Removing the inter-annual change parameters, the rest of the variables capture all kinds of influences including phenology, BRDF, topographic shadowing, etc. A Landsat image at any date can be predicted as:

$$\text{predict}(x) = a_0 + a_1 \cos\left(\frac{2\pi}{T}x\right) + b_1 \sin\left(\frac{2\pi}{T}x\right) + a_2 \cos\left(\frac{2\pi}{0.5T}x\right) + b_2 \sin\left(\frac{2\pi}{0.5T}x\right) \quad (3)$$

where,

- $x$  Day-of-year.
- $T$  Number of days per year ( $T = 365$ ).
- $a_0$  Coefficient represents overall surface reflectance
- $a_1, b_1$  Coefficients capture the annual changes of surface reflectance
- $a_2, b_2$  Coefficients capture the bimodal variations of surface reflectance for each year.

After estimating the models for each pixel and for each spectral band, it is possible to predict what the “next” Landsat image will look like at any location and any date if there is no snow, cloud, or cloud shadow (Fig. 9).

One question that arises is how well we predict future Landsat images. We test this by predicting images for dates of future acquisitions and comparing them with real images. For these comparisons it is important to exclude pixels that have undergone land cover change. To select only “stable pixels” (i.e. no land cover change), we again use the parameters from the time series model ( $\sqrt{a_{2,7}^2 + b_{2,7}^2} < 0.02$  and stable in the last clear observations see Eq. (2) for details). Several metrics have been used to assess the error of predicted Landsat images as compared to observed Landsat images (Table 1). Root Mean Square Error (RMSE) and Residual normalized by Mean reflectance (RM) has been used for error assessment separately by Gao et al. (2006) and Roy et al. (2008). We also use a conventional R-square metric. Both Gao and Roy’s algorithms use multi-temporal MODIS data and Landsat data to predict Landsat observations. Our CMFDA prediction only uses multi-temporal Landsat data and shows very small errors. Four clear Landsat ETM+ images acquired in different seasons were compared with the predicted images for the study area (Table 1). The prediction errors for autumn and winter images are smaller than those in spring and summer images. The spring and summer images are more difficult to predict because phenological change is large during these times.

### 3.6. Change detection algorithms

The basis of our methods is comparison of the predicted images with observed images to find change. Since we can make these comparisons for any date that has Landsat acquisitions, we are faced with a question regarding how many dates, or comparisons, to use. Ideally, a single comparison would be definitive. However, there is sufficient noise in the system due to factors like atmospheric haze, missed clouds or cloud shadows, that when using a single date for

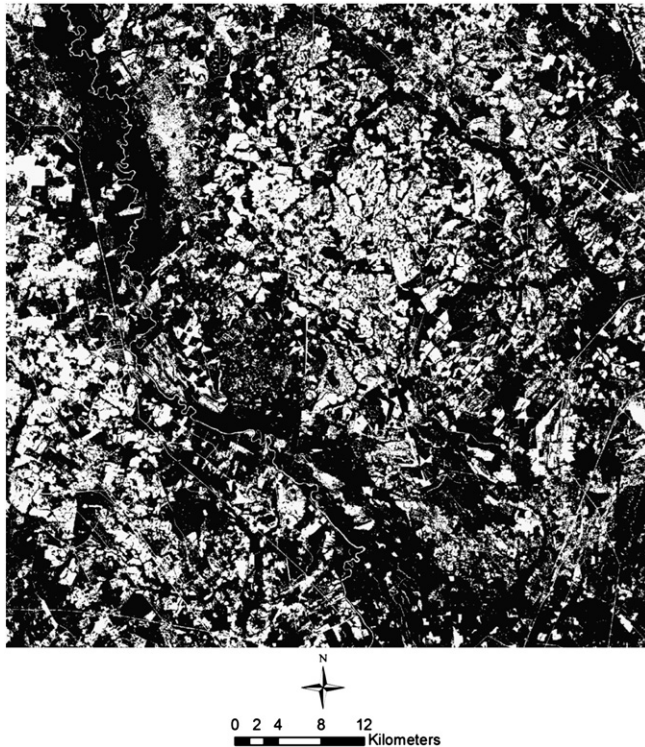


**Fig. 8.** Stable forest mask for the study area (white for disturbed or nonforested areas; black for stable forested areas).



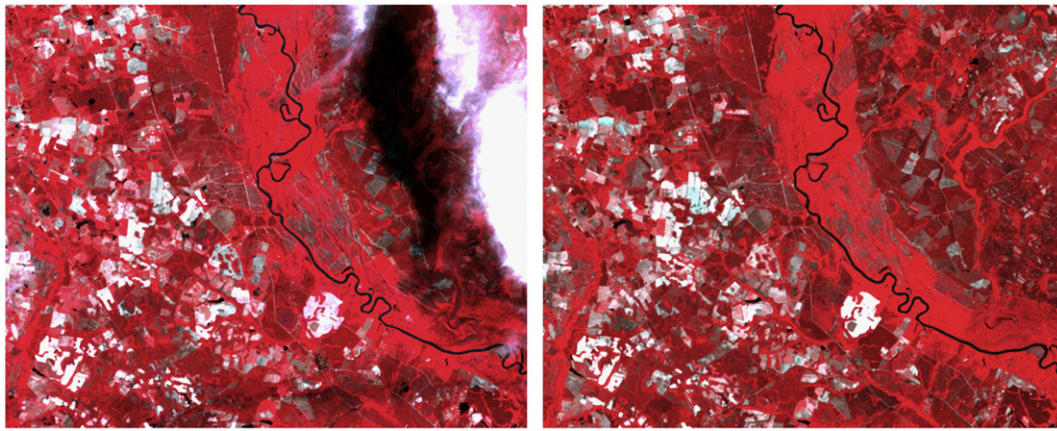


Fig. 9. (left) Observed and (right) predicted Landsat surface reflectances at a subset of the study area (shown with Bands 4, 3, and 2 in red, green, blue).

comparison, there are numerous false positives (false identification of forest disturbance). One approach to try to minimize this effect is to process a set of dates together as a group, as noise factors tend to be ephemeral in nature, but forest disturbance is persistent through time.

### 3.6.1. Single-date differencing algorithm

Ideally, if clouds, cloud shadows, and snow are well screened, the difference between the predicted and the observed image at the same day-of-year should be land cover change. However, omission of clouds and thick aerosols can lead to comparably large rates of false detection of forest disturbance. Fortunately, most of surface reflectance change caused by missed thin clouds or heavy aerosols behaves different spectrally from changes caused by forest disturbance. Though, in both of these situations, Band 1 and Band 7 surface reflectance will increase, the magnitude differs greatly. When forest is clear-cut or thinned, Band 7 will be strongly influenced while Band 1 will be only slightly changed (Healey et al., 2006), which is the opposite of the effect of thin cloud and thick aerosols. A ratio between increases in Band 7 and Band 1 can separate the noise effects (thin clouds and thick aerosols) from forest disturbance. Based on sensitivity analysis, a threshold of 3.0 for the ratio was used. Pixels with the ratio less than this threshold are ignored even if they show large difference in change indices.

Many different change indices have been developed for detecting forest disturbance. The simplest change index is the original surface reflectance. Healey et al. (2006) suggested the red band and SWIR bands are more sensitive to forest disturbance than the other Landsat optical bands. The most commonly used indices are from the Tasseled Cap Transformation (Crist, 1985; Crist & Ciccone, 1984) which reduces the six Landsat optical bands into three orthogonal indices – Brightness (B), Greenness (G), and Wetness (W), capturing the three major axes of spectral variation across the solar reflective spectrum. Wetness is particular useful in forest disturbance detection (Collins & Woodcock, 1996; Franklin et al., 2000). The Normalized Difference

Vegetation Index (NDVI) (Tucker, 1979) derived from TM Band 3 and Band 4 has been used extensively in many kinds of vegetation change detection algorithms. The Normalized Burn Ratio (NBR) has been used to assess the burn severity in Landsat images using Band 4 and Band 7. This index provides the best difference between health and burned vegetation (Howard et al., 2002). Recently, the newly developed Disturbance Index (DI) (Healey et al., 2005; Healey et al., 2006) has been used for large area Landsat forest disturbance detection (Masek et al., 2008). It is based upon the observation that cleared forest stands usually have a higher Brightness value and lower Greenness and Wetness values than forest stands. The DI transformation is a linear combination of the three Tasseled Cap indices re-scaled by the mean and standard deviation of the scene's forest value. As CMFDA models the phenology and BRDF effects in the data, we do not need to re-scale the DI by the mean and standard deviation. We simply used a linear combination of  $B-(G+W)$  as one of the tested change indices. We tested most of the indices discussed above, including: Band 3 surface reflectance, Band 7 surface reflectance, NDVI, NBR, Wetness, and  $B-(G+W)$ . Eq. (4) was applied to every pixel for the observed image and predicted image of the same day and this process was repeated for all available dates of Landsat data to identify forest disturbance. The  $B-(G+W)$  change index was used as it performed the best among all the tested change indices when a threshold of 0.18 was used for our study area (see Section 4.1.1. for detail).

Forest disturbance = stable forest mask is true and clear observation is true (Fmask)

$$\text{and } \frac{\text{obsB7} - \text{predB7}}{\text{obsB1} - \text{predB1}} > 3 \text{ and } (B - (G + W))_{\text{obs}} - (B - (G + W))_{\text{pred}} > 0.18 \quad (4)$$

As we are identifying the disturbance pixels using a single observation, the only criterion that determines whether a pixel has

Table 1

R<sup>2</sup>, RM, and RMSE for predicted Landsat images at different seasons. For each spectral band, the highest R<sup>2</sup>, smallest RMSE and RM are in bold.

Time	Spring (04/26/2001)			Summer (06/16/2002)			Autumn (10/06/2002)			Winter (01/04/2001)		
	R <sup>2</sup>	RM	RMSE	R <sup>2</sup>	RM	RMSE	R <sup>2</sup>	RM	RMSE	R <sup>2</sup>	RM	RMSE
Band 1	<b>0.89</b>	0.19	0.006	0.84	0.16	0.006	0.83	<b>0.13</b>	<b>0.004</b>	<b>0.89</b>	<b>0.13</b>	<b>0.004</b>
Band 2	0.91	0.2	0.009	0.87	0.16	0.01	0.9	<b>0.08</b>	<b>0.004</b>	<b>0.92</b>	0.09	0.005
Band 3	<b>0.94</b>	0.22	0.009	0.89	0.26	0.014	0.89	0.17	<b>0.006</b>	<b>0.94</b>	<b>0.11</b>	0.007
Band 4	<b>0.91</b>	0.04	0.016	0.89	0.07	0.027	0.89	<b>0.03</b>	<b>0.012</b>	0.9	0.06	0.014
Band 5	0.95	0.1	0.018	0.91	0.08	0.018	0.94	<b>0.05</b>	<b>0.011</b>	<b>0.97</b>	0.06	0.013
Band 7	0.95	0.14	0.014	0.91	0.17	0.019	0.91	<b>0.1</b>	0.01	<b>0.96</b>	<b>0.09</b>	0.011



changed or not is the change magnitude of the index and a fixed Band 7/Band 1 ratio. Therefore the single-date differencing algorithm is sometimes affected by ephemeral noise and causing relatively large commission errors in change detection. Moreover, at different locations and for different forest types, the magnitude of the change threshold may differ, and the Band 7/Band 1 ratio test may fail, leading to lower accuracy for the single-date differencing algorithm. A method based on multi-date observations may solve these problems.

### 3.7. Multi-date differencing algorithm

One way to help reduce the effect of noise factors on commission errors (false forest change) is to use multiple observations through time. If a pixel is observed to change in multiple successive images, it is more likely to be forest disturbance. The multi-date differencing algorithm determines a disturbance pixel by the number of times that observed and predicted images differ more than a threshold in successive images. Pixels showing change for one or two times will be flagged as “probable change”. If a third consecutive change is found, the pixel is assigned to the “change” class. Optimal results were obtained when  $B-(G+W)$  was used as change index with a threshold of 0.12 (see Section 4.2.1. for detail). The details of the multi-date differencing algorithm are presented in Eq. (5).

$$\begin{aligned} \text{Forest disturbance} &= \text{stable forest mask is true and clear observation} \\ &\text{is true(Fmask)} \\ &\text{and 3 consecutive observations with } (B-(G+W))_{\text{obs}} \\ &\quad - (B-(G+W))_{\text{pred}} > 0.12 \end{aligned} \quad (5)$$

Notice that its optimal threshold is 0.06 less than the single-date differencing algorithm. With a lower threshold, very subtle changes (forest thinning) will be identified. Thanks to the addition of the temporal dimension, most of the commission errors were excluded by the need for consecutive observations to exceed the threshold (see Section 4.2.2 for details). Also, the empirically derived Band 7/Band 1 relationship is no longer necessary. Considering all these benefits from using consecutive observations, the multi-date differencing algorithm was chosen as the final CMFDA result, and the single-date differencing algorithm was used only for finding changes in the last clear observation in defining stable forest mask.

### 3.8. Accuracy assessment

#### 3.8.1. Reference map

Maps derived from remotely-sensed imagery should always be assessed for accuracy against an independent dataset that is closer to the truth. This independent dataset is usually from in situ field work or manual interpretation of finer resolution images like IKONOS or QuickBird. In this study, not only do we need to determine where disturbance occurs but also when. As there are no independent datasets available that have finer spatial resolution and higher temporal frequency than Landsat images, the reference data were derived from manual interpretation of the original Landsat images (Cohen et al., 2010). High spatial resolution images from Google Earth (<http://earth.google.com/>) were used to help the manual interpretation. Though the high spatial resolution images in Google Earth cannot provide the same temporal frequency as Landsat TM/ETM+, their high spatial resolution is helpful in separating forest, nonforest, and disturbance at longer time intervals. Two types of forest disturbance (clear-cut and thinning) were included in this reference dataset. The partial cuts and clear-cuts are quite easy to identify in the high spatial resolution images in Google Earth, as the details of the individual trees can be clearly seen. False color composites of Landsat Band 4, Band 3, and Band 2 surface reflectances were used to visualize the different types of disturbances (see Fig. 1 for example). In these images,

mature forests appear dark red, while clear-cut areas show bright white color and the partial cut locations are less dark red. We chose 21 rectangular areas that contain forest disturbance patches of different sizes and include other land cover classes to train and evaluate the algorithm. All chosen rectangular areas, each with width and length larger than 3 km, were carefully interpreted to determine precisely the location and timing of forest disturbance.

Two steps were used to produce the final disturbance reference map. First, an annual disturbance map was generated by visually comparing the last clear Landsat image in 2002 and the last clear Landsat image in 2003. Forest disturbance that occurred in 2003 should be captured in this annual disturbance map. If there was confusion in comparing the two Landsat images, high spatial resolution images before and after 2003 (can be a few years apart) from Google Earth were used to help determine what was happening at the specific locations. In the worst case, if both high spatial resolution images from Google Earth and the Landsat images pairs do not support a confident decision, the time series of surface reflectances were used to better identify the disturbed pixels (Fig. 10).

The timing of the disturbance was derived by careful interpretation of all available Landsat TM/ETM+ images acquired in 2003 (a total of 24 images with cloud cover less than 90%). Within each rectangular area, the interpreter sorted through all the TM/ETM+ images carefully. The disturbance date is the first time when forest changes are found and it is determined by visually comparing each pair of consecutive images. The result is a set of reference rectangles that show the location of forest disturbance that occurred in 2003, labeled with the date when the disturbances were first observed (Fig. 11). These sites then serve as our reference data to train and evaluate CMFDA.

We divided the reference rectangles into two groups: one group used for training CMFDA, that is, to find the optimal change index, threshold, and number of consecutive observations; one group used for evaluating CMFDA accuracy. The reference rectangles were sorted and ranked by size and the odd number ranked rectangles (in blue) were used for help training CMFDA, and the even number ranked rectangles (in red) were used for evaluating CMFDA (Fig. 11). The goals of this approach were to roughly divide the reference data in half for training and testing, and to avoid bias by making sure that entire polygons were either training or testing, but not both (Friedl et al., 2000).

#### 3.8.2. Definitions of accuracy

Considering the misregistration errors in the Landsat images and especially the ambiguity in validating disturbance at the edge of the change patches, pixels located on the edges of the disturbance polygons (within 1 pixel of the border) were not included in accuracy assessment. As the disturbance map has both spatial and temporal information, we assessed the spatial and temporal map accuracies separately. We think the spatial accuracy is more important than temporal accuracy, as omission and commission of disturbance is more serious than finding disturbance later than the reference map. Overall map accuracy is not a very useful measure in this case as the proportion of forest change is small and therefore the accuracy of the forest change class would not contribute significantly to the overall accuracy. Instead, the producer's and user's accuracies for the forest disturbance class in Eqs. (6) and (7) were more important for evaluating the algorithm. Basically, with higher producer's accuracy, there will be fewer omission errors and with higher user's accuracy, fewer commission errors (Congalton, 1991).

$$\text{producer's accuracy} = \frac{\text{num of correctly identified disturbance pixels}}{\text{num of disturbance pixels in reference map}} \quad (6)$$

$$\text{user's accuracy} = \frac{\text{num of correctly identified disturbance pixels}}{\text{num of disturbance pixels in algorithm map}} \quad (7)$$

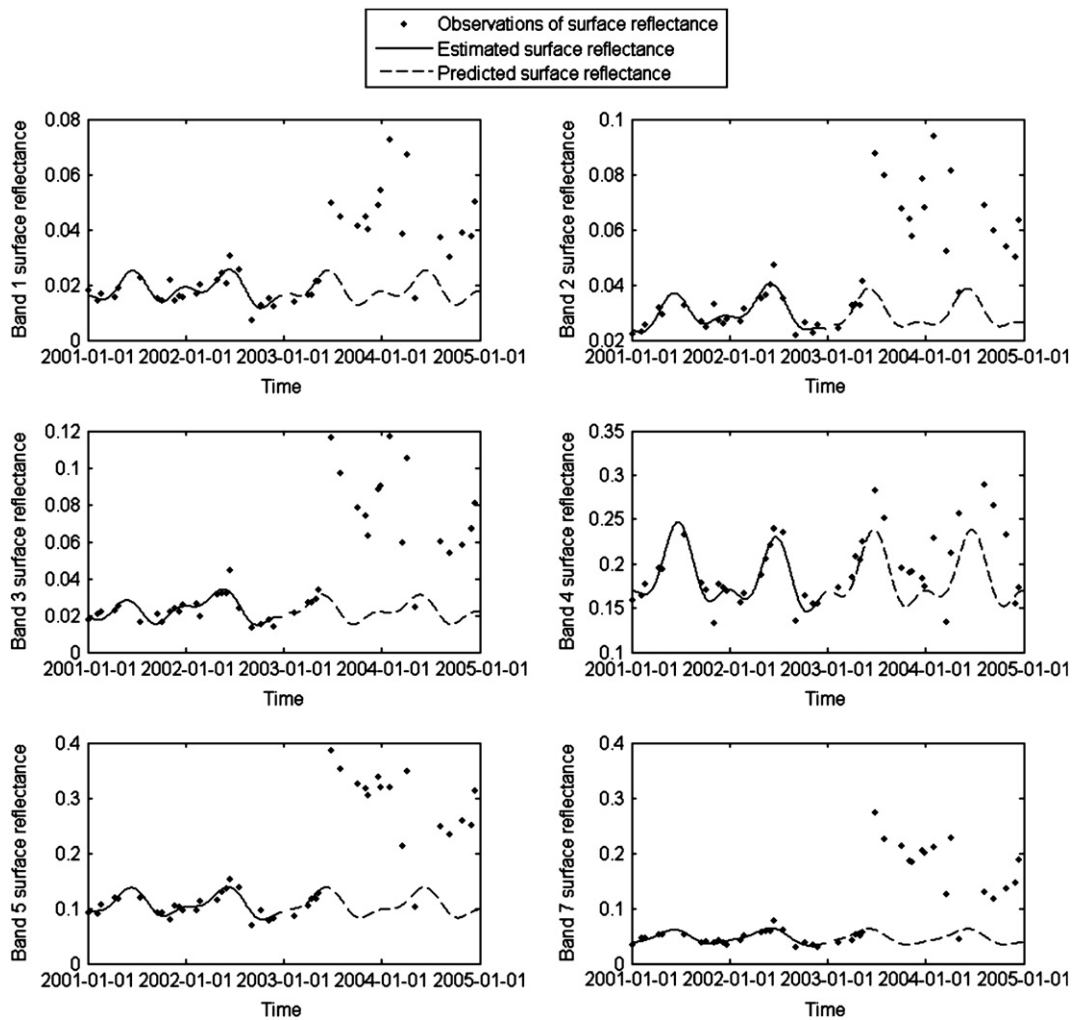


**Fig. 10.** Time series data of a typical disturbed deciduous forest pixel for all 6 optical Landsat surface reflectance bands. Persistent changes are easily identified by comparing the predicted surface reflectances and the observed clear surface reflectances.

Temporal accuracy is evaluated for the forest disturbance pixels that are correctly identified spatially. With the temporally dense Landsat images, forest thinning may be observed before a forest clear-cut as clear-cutting may need a few weeks to finish. It is difficult to determine the disturbance time for this kind of subtle change before a clear-cut. The reference map labels a disturbance time when the disturbance is initially observed with high confidence by the interpreter. However, CMFDA can find very subtle changes at the very beginning of the disturbances. Therefore, the algorithm occasionally finds disturbances earlier than the reference map, which is not considered a mistake, but rather the limitation of manual interpretation in defining subtle changes. We think the algorithm is correct temporally if the disturbance time found by CMFDA is earlier or equal to the disturbance time in the reference map and the temporal accuracy is calculated with Eq. (8).

$$\text{temporal accuracy} = \frac{\text{num of pixels}(\text{algorithm time} \leq \text{reference time})}{\text{num of correctly identified disturbance pixels}} \quad (8)$$

The producer's/user's accuracies in the spatial domain and the temporal accuracy were used to find the best change index, its optimal threshold, and the number of successive clear observations to use for change identification.

## 4. Results

### 4.1. Single-date differencing algorithm results

#### 4.1.1. Selecting a change index and thresholds

The odd number ranked rectangles were used for helping select a change index and thresholds for the single-date differencing algorithm. In Fig. 12 the spatial user's and producer's accuracies and the temporal accuracy are plotted as a function of the threshold used for different change indices. We use the intersection of the producer's and the user's accuracies as the "best" threshold, as it balances errors of omission and commission. The Disturbance Index B-(G+W) performed the best among all the tested change indices. When the threshold of 0.18 was used for the change in the Disturbance index, both the producer's and user's accuracies were around 90%, and the temporal accuracy is around 85%. The spatial accuracies of the other five tested indices are slightly lower, but are all above 88%. The temporal accuracies are also related to the thresholds used for defining change, usually the higher the threshold, the later the captured change, which leads to lower temporal accuracies. For most of the indices the temporal accuracies are around 85%, except for the two indices (NDVI and NBR) that use the NIR band as its main input. The NIR surface reflectance varies significantly with vegetation phenology, which may induce problems in determining the time of detected changes and reduce the temporal accuracies.

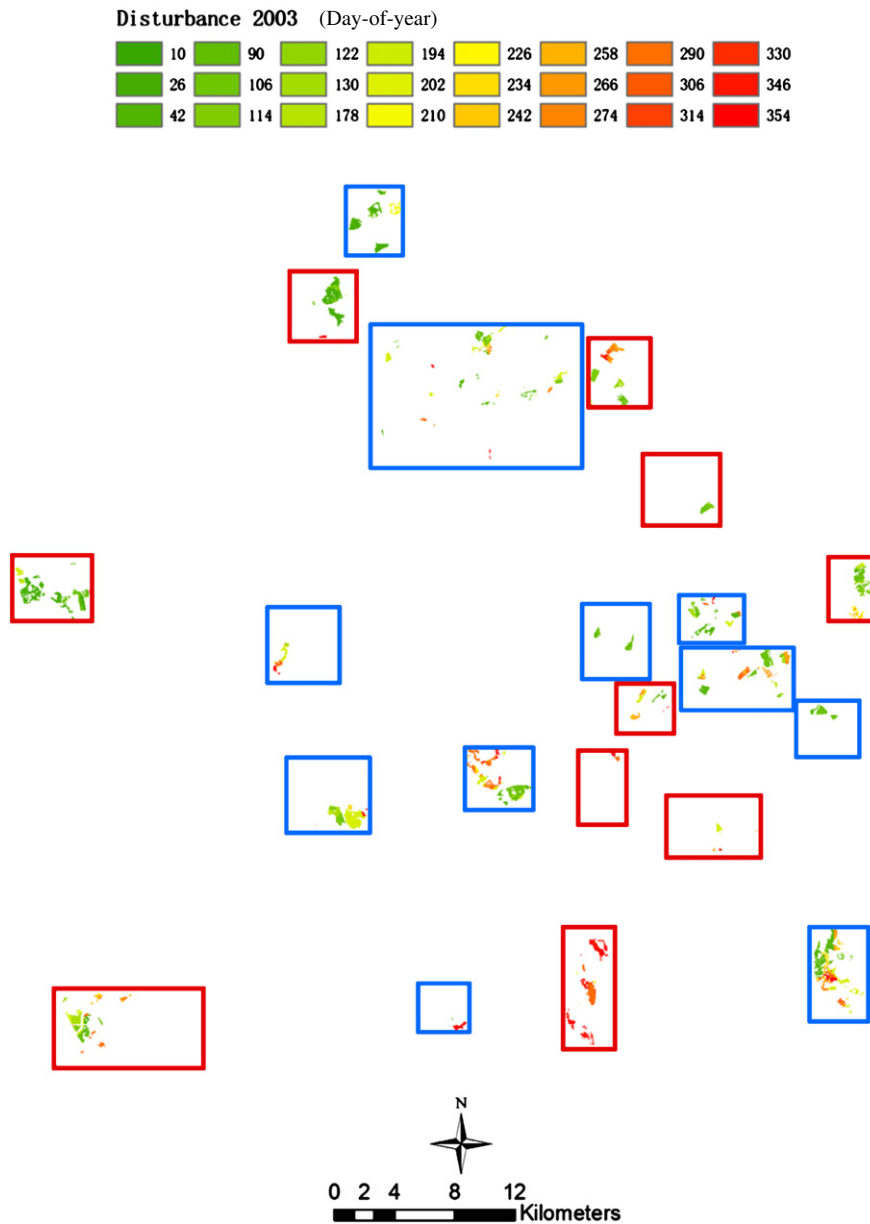


**Fig. 11.** Reference map for forest disturbance in 2003 at study area. The blue reference rectangles were used for training and the red ones were used for evaluating the accuracy of CMFDA.

#### 4.1.2. Testing on unseen reference data

The even number ranked rectangles were used to evaluate the accuracy of the single-date differencing algorithm with  $B-(G+W)$  as its change index and a threshold of 0.18. The confusion matrix of spatial accuracies is shown in Table 2. Both the user's and producer's accuracies for forest disturbance are more than 93%, and producer's accuracy is slightly higher than the user's accuracy. The temporal accuracy of those spatially corrected identified forest disturbance pixels is about 90%.

#### 4.2. Multi-date differencing algorithm results

##### 4.2.1. Selecting the number of successive observations and thresholds

The effects of using multiple consecutive dates as part of the change detection with  $B-(G+W)$  as the tested change indices are shown in Fig. 13. Fig. 13 (top) shows the spatial accuracies (both user's and producer's) for different change thresholds and different lengths of successive identifications of change for the same pixel.

The highest accuracy is achieved from three successive clear observations with a threshold of 0.12. In this best scenario, the producer's and user's accuracies in the spatial domain are around 95% and the temporal accuracy is approximately 93%. Due to the relatively large number of commission errors when using only one clear observation, the user's accuracy is too low to be shown in Fig. 13 (top). Though the optimal threshold is 0.06 less than the single-date differencing algorithm, its commission error is lower (higher user's accuracy). The spatial accuracies are relatively robust to this optimal threshold when three consecutive clear observations are used. The temporal accuracies are related to the change thresholds and the number of successive observations, usually the higher the threshold or the larger number of successive observations, the later the captured change, and lead to lower temporal accuracies. Generally, the temporal accuracies for multi-date differencing algorithms are all high (more than 85%) when the threshold varies greatly (from 0.08 to 0.16) and they are not very sensitive to the number of successive observations used (Fig. 13 (bottom)).



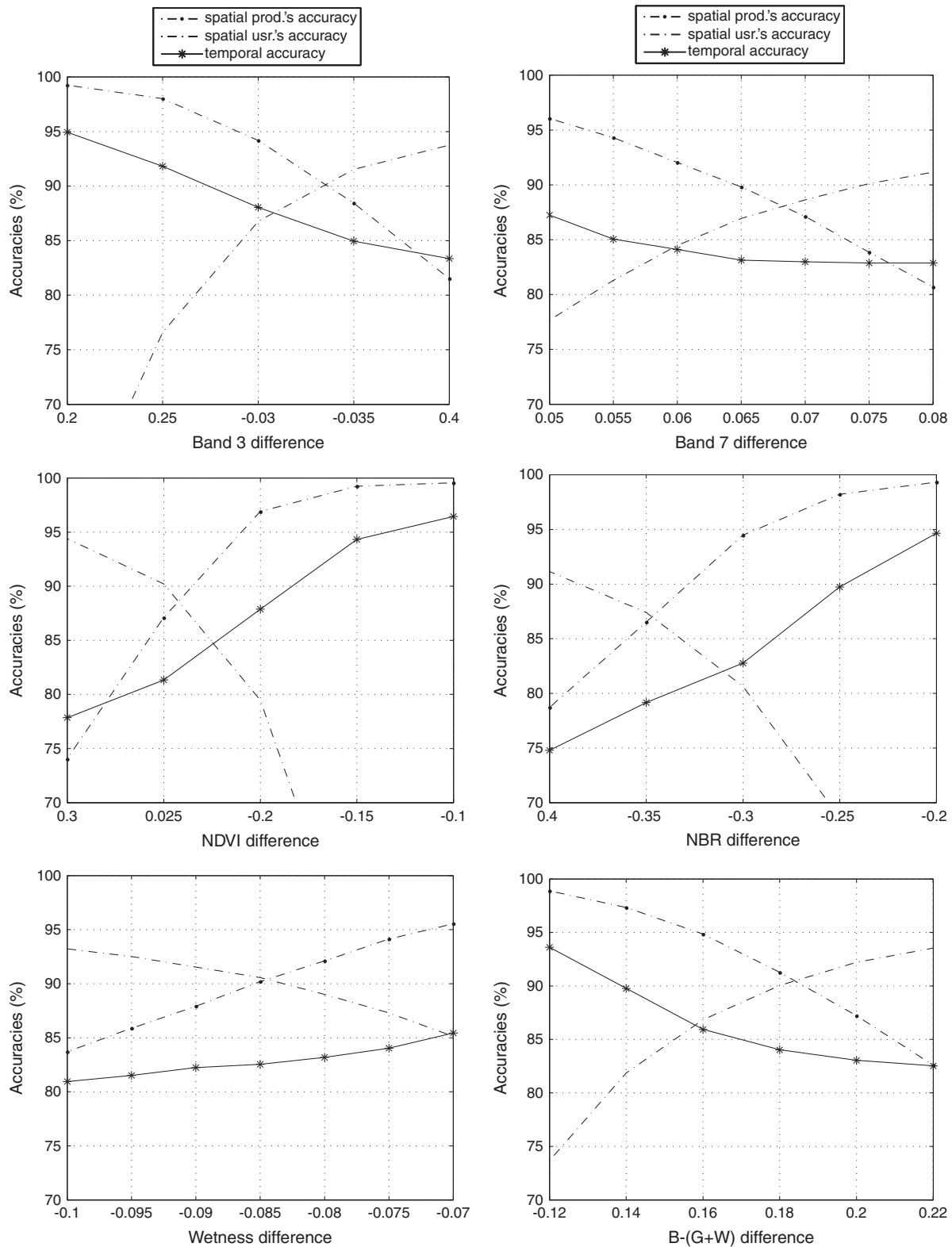


Fig. 12. Accuracies for the single-date differencing algorithm for the six different change indices.

#### 4.2.2. Testing on unseen reference data

Similarly, the even number ranked rectangles were used to evaluate the accuracy of the multi-date differencing algorithm with  $B-(G+W)$  as its change index, a threshold of 0.12, and three consecutive observations. The confusion matrix of spatial accuracies is shown in Table 3. Both the user's and producer's accuracies for forest disturbance are more than 95%, and producer's accuracy is also higher than the user's

accuracy. The temporal accuracy of the correctly identified forest disturbance pixels is almost 94%.

The map derived from multi-date differencing algorithm shows locations and dates of forest disturbance during in 2003 (Fig. 14). The colors of the polygons represent the first date the forest disturbance is captured by the algorithm using all available Landsat images. Within all the 21 reference rectangles, the multi-date differencing

**Table 2**

Confusion matrix for the accuracy assessment of the single-date differencing algorithm. The overall accuracy results are not terribly revealing, as after excluding the edges of the change polygons, the change pixels left are only about 3% of the total interpreted pixels.

Reference data				
Single-date differencing	Forest disturbance	Others	Total	User's (%)
Forest disturbance	7422	523	7945	93.42
Others	492	241,969	242,461	99.80
Total	7914	242,492	250,406	
Producer's (%)	93.78	99.78	Overall (%)	99.59

results and the reference map are very similar. However, at this  $60 \times 60$  km scale, it is difficult to find any significant differences between the reference map and the map derived by the algorithm. Looking closer at three reference rectangles used for testing (Fig. 15), the disturbance map derived from the algorithm agrees closely with the disturbance found in the reference map both spatially and temporally (green color). The three types of disagreements (blue, violet, and red) are all distributed at the edges of disturbance

**Table 3**

Confusion matrix for the accuracy assessment of the multi-date algorithm. The overall accuracy results are not terribly revealing, as after excluding the edges of the change polygons, the change pixels left are only about 3% of the total interpreted pixels.

Reference data				
Multi-date differencing	Forest disturbance	Others	Total	User's (%)
Forest disturbance	7653	333	7985	95.83
Others	261	242,159	242,420	99.89
Total	7914	242,492	250,406	
Producer's (%)	96.70	99.86	Overall (%)	99.76

patches. These false identifications are mainly caused by the misregistration in the image stack and problems in interpreting forest disturbance at the boundaries of patches.

## 5. Discussion and conclusions

In this study, we developed a new change detection algorithm for continuous monitoring of forest disturbance at high temporal frequency. This approach also allows construction of a history of forest

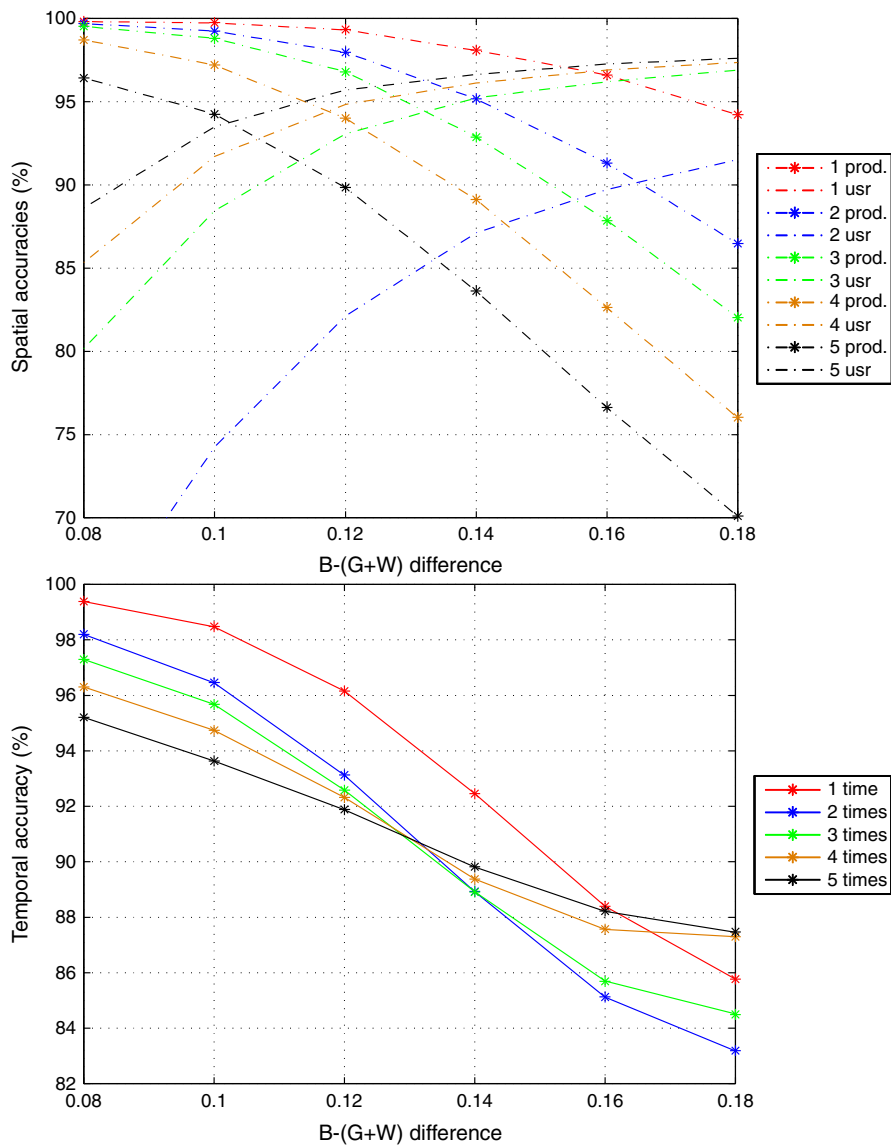


**Fig. 13.** (top) Spatial and temporal (bottom) accuracies of the multi-date differencing algorithm for different combinations of numbers of succession observations of change and change index thresholds. Notice that the intersection of user's and producer's accuracies get maximum for 3 consecutive observations.

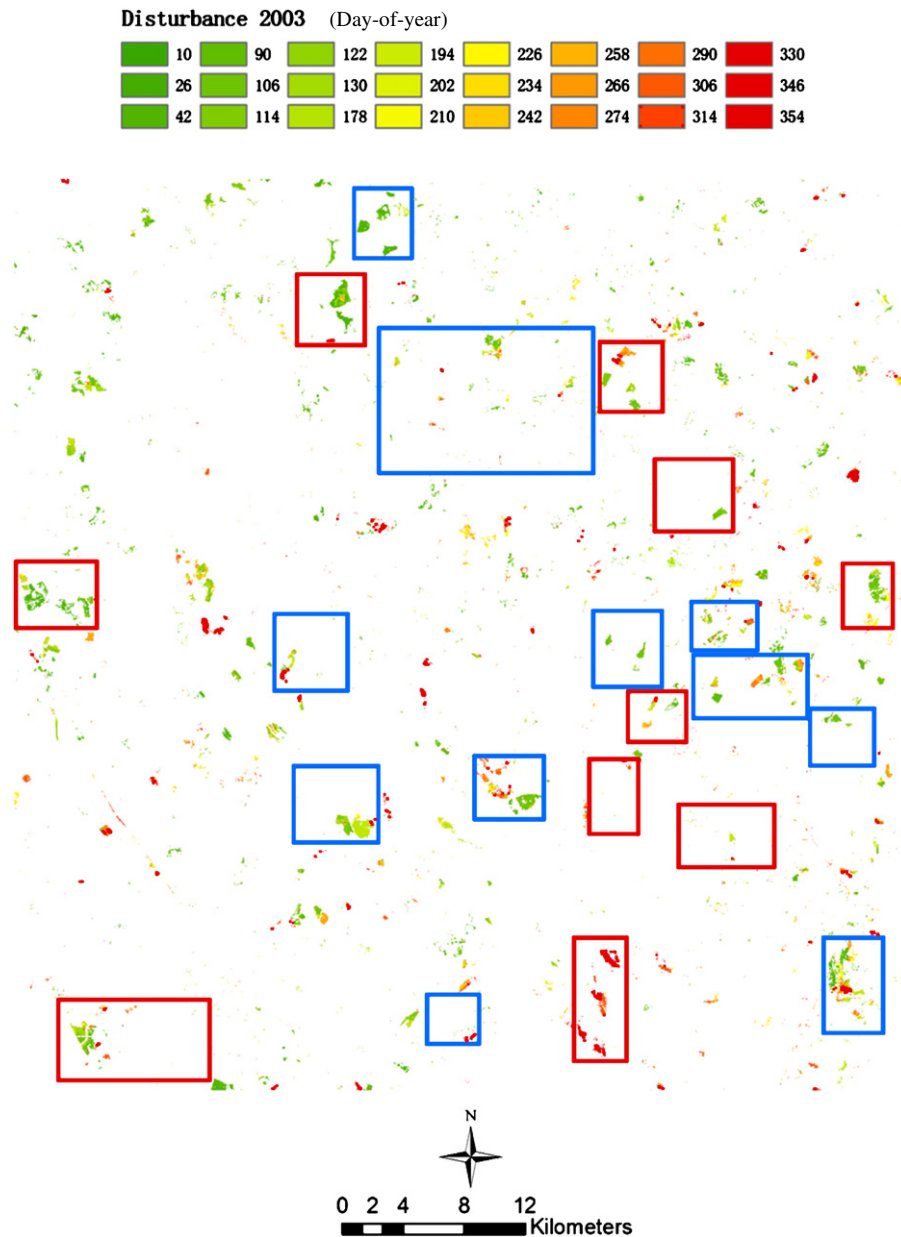
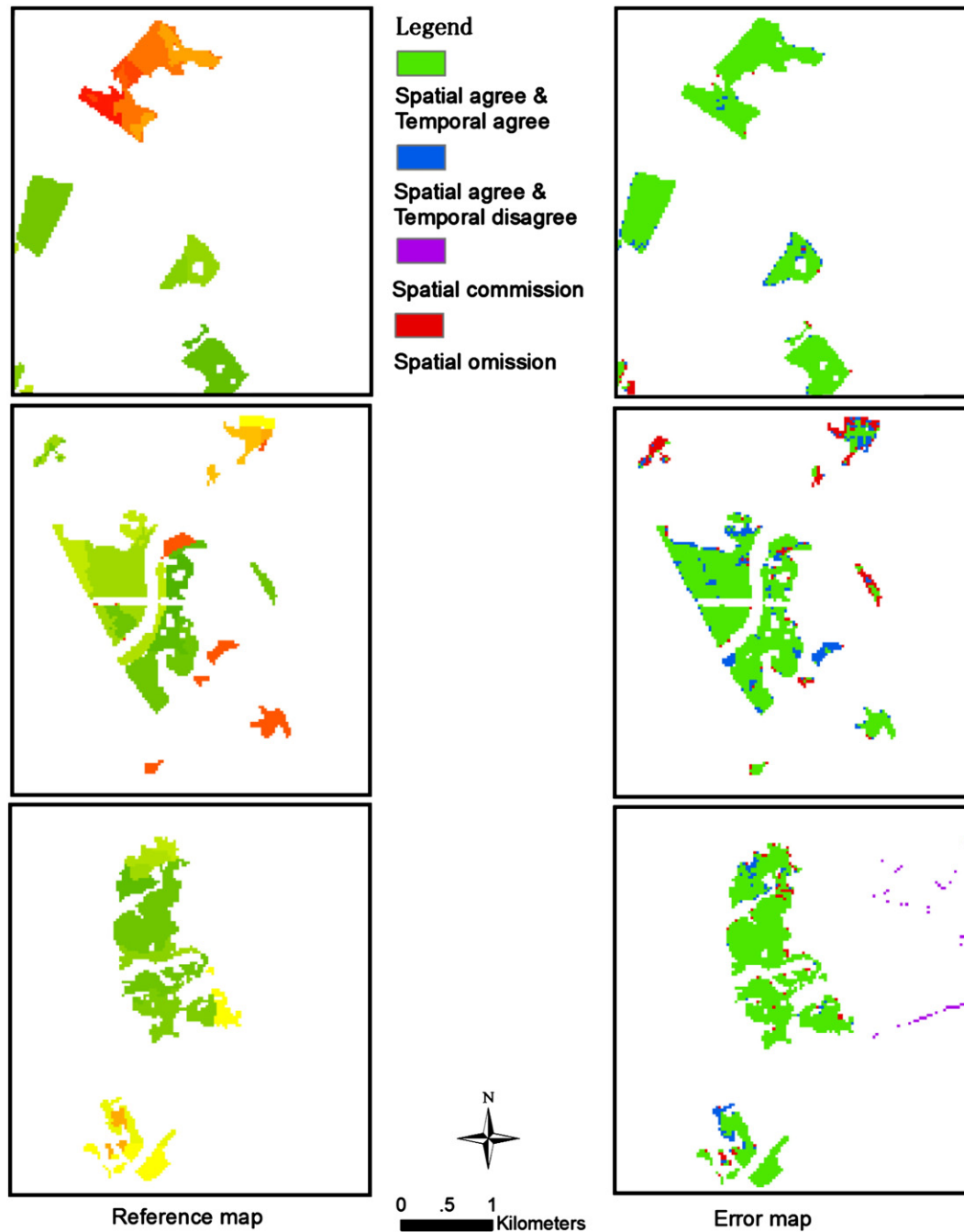


Fig. 14. Multi-date differencing algorithm map for forest disturbance in 2003 at study area.

disturbance. Using all the available Landsat ETM+ images in two years, models using sines and cosines are fit for each pixel and each spectral band. These models can predict Landsat images at any date assuming there is not any land cover change. CMFDA flags forest disturbance by differencing the predicted and observed Landsat images. We tested two algorithms called single-date and multi-date differencing for detecting forest disturbance. The multi-date differencing algorithm was chosen as the final change detection method for CMFDA due to its higher spatial and temporal accuracies. It uses  $B-(G+W)$  as its change index and a threshold of 0.12 for defining “change”. It determines a disturbance pixel by the number of times “change” is observed consecutively. Pixels showing “change” for one or two times are flagged as “probable change”. If a third consecutive “change” is found, the flag will be mapped as forest change. The reference map revealed that the CMFDA result is accurate in detecting forest disturbance both spatially and temporally at the tested Savannah River site, with producer's and user's accuracies higher than 95% and temporal accuracy of approximately 94%.

CMFDA has many advantages. It can be fully automated and has the potential of monitoring forest disturbance continuously as new images are collected. Though a predefined change threshold is used at this specific study site, sensitivity analysis suggests this algorithm is relative robust to this threshold when three consecutive clear observations are used. The continuous character of the monitoring makes the algorithm capable of identifying disturbance soon after Landsat observations become available. Therefore, how fast the CMFDA is able to find change accurately is solely dependent on the frequency of available clear observations. The potential to use the methods presented here for monitoring surface change will improve as the frequency of high resolution images from sensors like Landsat become more available (Arvidson et al., 2006). The first major step forward in this domain was the opening of the US archive so that the vast holding of Earth Resources Observation and Science (EROS) Data Center can be used. With regard to future observations, the launch of the Landsat Data Continuity Mission (LDCM) should greatly increase the frequency of available observations as the duty cycle for LDCM is larger than any of the previous





**Fig. 15.** Zoom in of reference and error maps. The colors in reference map show the disturbance time (same legend in Fig. 14). The colors in accuracy map show different types of errors (see legend of this figure).

Landsat satellite. More importantly, when the two Sentinel 2A/2B satellites are launched, they will have a repeat time of every five days. When combined with LDCM data, there would be as many as 8 high resolution observations per month, which will greatly improve the availability of observations such that we will be able to begin to monitor change in near real time (a week or two in many parts of the world).

By considering each pixel separately, CMFDA can overcome most of the limitations that the conventional approaches have. By using any clear observations for each pixel to track spectral trends over time, CMFDA expands the use of Landsat images to any time of year and to all kinds of conditions (e. g., cloud, snow, heavy aerosols). As CMFDA fits models for each pixel, it can work in heterogeneous forest

areas which are reported to be problematic for the scene-based normalized change indices such as IFZ and DI (Huang et al., 2010; Masek et al., 2008). The problem caused by the failure of the Scan Line Corrector (SLC) in Landsat 7 is not nearly as significant for CMFDA as compared with more conventional approaches. The scan line gaps are treated just like clouds or other things that remove observations from images and the available good observations are used. One area of future research will be to integrate observations from adjacent Landsat images in the zone of “side lap”. This approach will further minimize the effects of Landsat 7 SLC-off gaps as they are most pronounced in these areas of side lap. The same is true for images with partial cloud cover, as they have many useful observations. As a result, it would be highly desirable if the Landsat satellites of the

future collected all possible observations, as even partially cloudy images have value in analysis systems like CMFDA.

CMFDA also has limitations. First of all, CMFDA works better with larger number of observations. However, areas outside the U.S. may not have enough observations, particularly for some years in the 1980s and 1990s (Goward et al., 2006). Luckily, the new acquisition strategies for Landsat 7 (Arvidson et al., 2001; Arvidson et al., 2006) provide more frequent observations. The years between 1999 and early 2003 might be considered as the “golden years” for estimating models for CMFDA, as during this time both Landsat 5 and Landsat 7 are functioning normally. Therefore, we could build models for each pixel during this period and flag future changes. Similarly, we can detect changes that occurred in the 1980s and 1990s as long as there are data available using the models calibrated in the “golden years”, by running the time series analysis backward in time. The second limitation of CMFDA is the computation time associated with creating models to predict future surface reflectance. The two-step cloud/cloud shadow, and snow masking is critical, as including noise factors in the data undermines the entire process. However, when the prediction models are ready, CMFDA is able to update a disturbance map as soon as a new Landsat observation is acquired. This process is very fast and does not require reanalysis of the historical data. Such an approach points to the possibility of processing images in CMFDA as part of the process for ingesting new images, paving the way for monitoring land cover change as close as possible to when it happens using Landsat data. A third limitation is that the methods proposed above are all based on the assumption that land cover change only occurs once in the detection period which is not true if the detection period is longer than some of the “permanent change” like forest disturbance. Masek et al. (2008) suggested that the highest forest disturbance cycle time is approximately 5 years. To include changes of this frequency, CMFDA needs to re-estimate the surface reflectance models using the newest data available at 5 years intervals. Finally, though CMFDA identifies forest disturbance much quicker than the conventional approaches, the expected time to find “probable change” and “change” in CMFDA is still too long to monitor changes as they are occurring. Assuming cloud probability of 50%, CMFDA will typically need at least half a month to find “probable change” and one and a half months to find “change” in places with the most frequent observations like United States. It will take longer in other parts of the world due to less frequent Landsat observations. To achieve the goal of global near-real time monitoring of land cover change, using more Landsat-like sensors or fusion with higher temporal frequency sensors like MODIS (Hilker et al., 2009) are choices in future studies.

This study is a “prototype” for monitoring forest disturbance continuously with high temporal frequency. The robustness of this approach has not been tested in other areas. Therefore, there is still much work needed. Expansion of the study to other regions will undoubtedly result in improvements to the approach because of the differences in forest types, tree density, composition of species, and background (rocks/soil). One area of future work will be to broaden the variety of models used for the temporal trajectory of surface reflectance. While combinations of sines and cosines worked well in this situation, there will be a need for other models in other locations. There is no reason a whole family of models couldn't be tested for each pixels and the best model selected.

In this first use of this approach we estimated the models on the years 2001 and 2002 and applied the model to 2003. When looking retrospectively (to reconstruct the history of forest disturbance) it will be possible to look at much longer time series of images and select a set of years that do not exhibit change for calibrating the surface reflectance models that are then applied to other years. In this case, there is no reason to constrain all pixels in an area to being estimated on the same set of years. This approach will in some ways simplifying both the estimating of the surface reflectance models and their usage

as they won't be complicated by change near the beginning or end of the estimating period. Moreover, CMFDA has the potential of monitoring other land cover changes if a specific predefined land cover mask can be derived accurately. For instance, it is possible to identify wetland loss by finding changes within a predefined wetland map, or if we are looking for changes in agriculture land use, we may be able to monitor agriculture abandonment. Further studies are necessary for detecting other land cover changes using algorithms similar as CMFDA.

## References

- Arvidson, T., Gasch, J., & Goward, S. N. (2001). Landsat 7's long-term acquisition plan - an innovative approach to building a global imagery archive. *Remote Sensing of Environment*, 78(1–2), 13–26.
- Arvidson, T., Goward, S., Gasch, J., & Williams, D. (2006). Landsat-7 long-term acquisition plan: Development and validation. *Photogrammetric Engineering and Remote Sensing*, 72(10), 1137–1146.
- Bolton, D. K., & Woodcock, C. E. (in preparation). Detecting hemlock woolly adelgid damage in the northeast US with a dense timeseries of Landsat data.
- Cohen, W. B., Fiorella, M., Gray, J., Helmer, E., & Anderson, K. (1998). An efficient and accurate method for mapping forest clear cuts in the Pacific Northwest using Landsat imagery. *Photogrammetric Engineering and Remote Sensing*, 64(4), 293–300.
- Cohen, W. B., Yang, Z., & Kennedy, R. (2010). Detecting trends in forest disturbance and recovery using yearly Landsat time series: 2. TimeSync – Tools for calibration and validation. *Remote Sensing of Environment*, 114(12), 2911–2924.
- Coiner, J. C. (1980). Using Landsat to monitor changes in vegetation cover induced by desertification processes. *Symposium on Remote Sensing of the Environment*, 3(14), 1341–1347.
- Collins, J. B., & Woodcock, C. E. (1996). An assessment of several linear change detection techniques for mapping forest mortality using multitemporal Landsat TM data. *Remote Sensing of Environment*, 56, 66–77.
- Congalton, R. (1991). A review of assessing the accuracy of classifications of remotely sensed data. *Remote Sensing of Environment*, 37(1), 35–46.
- Coppin, P. R., & Bauer, M. E. (1994). Processing of multitemporal Landsat TM imagery to optimize extraction of forest cover change features. *IEEE Transactions on Geoscience and Remote Sensing*, 32(4), 918–927.
- Crist, E. P. (1985). A TM tasseled cap equivalent transformation for reflectance factor data. *Remote Sensing of Environment*, 17, 301–306.
- Crist, E., & Cicone, R. C. (1984). A physically-based transformation of thematic mapper data – The TM Tasseled Cap. *IEEE Transactions on Geoscience and Remote Sensing*, 22, 256–263.
- Davis, J. C. (1986). *Statistics and data analysis in geology* (Second Edition). New York, N. Y.: J. Wiley and Sons 646.
- DuMouchel, W. H., & O'Brien, F. L. (1989). *Integrating a robust option into a multiple regression computing environment*. *Computer Science and Statistics: Proceedings of the 21st Symposium on the Interface*. Alexandria, VA: American Statistical Association.
- Franklin, S. E., Moskal, L. M., Lavigne, M. B., & Pugh, K. (2000). Interpretation and classification of partially harvested forest stands in the Fundy model forest using multitemporal Landsat TM digital data. *Canadian Journal of Remote Sensing*, 26(4), 318–333.
- Friedl, M., Woodcock, C. E., Gopal, S., Muchoney, D., Strahler, A. H., & Barker-Schaaf, C. (2000). A note on procedures used for accuracy assessment in land cover maps derived from AVHRR data. *International Journal of Remote Sensing*, 21(5), 1073–1077.
- Gao, F., Masek, J., Hall, J., & Schwaller, M. (2006). On the blending of the Landsat and MODIS surface reflectance: Predicting daily Landsat surface reflectance. *IEEE Transactions on Geoscience and Remote Sensing*, 44(8), 2207–2219.
- Garcla-Haro, F. J., Gilabert, M. A., & Meli, Á. (2001). Monitoring fire-affected areas using Thematic Mapper data. *International Journal of Remote Sensing*, 22(4), 533–549.
- Goodwin, N. R., Coops, N. C., Wulder, M. A., Gillanders Schroeder, T. A., & Nelson, T. (2008). Estimation of insect infestation dynamics using a temporal sequence of Landsat data. *Remote Sensing of Environment*, 112, 3680–3689.
- Goward, S., Arvidson, T., Williams, D., Faundeen, J., Irons, J., & Franks, S. (2006). Historical record of Landsat global coverage: mission operations, NSLRSDA, and international cooperator stations. *Photogrammetric Engineering and Remote Sensing*, 72(10), 1155–1169.
- Hayes, D. J., & Sader, S. A. (2001). Comparison of change-detection techniques for monitoring tropical forest clearing and vegetation regrowth a time series. *Photogrammetric Engineering and Remote Sensing*, 67(9), 1067–1075.
- Healey, S. P., Cohen, W. B., Yang, Z., & Krankina, O. N. (2005). Comparison of Tasseled Cap-based Landsat data structure for use in forest disturbance detection. *Remote Sensing of Environment*, 97, 301–310.
- Healey, S. P., Yang, Z., Cohen, W. B., & Pierce, D. J. (2006). Application of two regression-based methods to estimate the effects of partial harvest on forest structure using Landsat data. *Remote Sensing of Environment*, 101, 115–126.
- Hilker, T., Wulder, M. A., Coops, N. C., Linke, J., McDermind, G., Masek, J. G., Gao, F., & White, J. C. (2009). A new data fusion model for high spatial- and temporal-resolution mapping of forest disturbance based on Landsat and MODIS. *Remote Sensing of Environment*, 113, 1613–1627.
- Holland, P. W., & Welsch, R. E. (1977). Robust regression using iteratively reweighted Least-Squares. *Theory and Methods*, 813–827.
- Hostert, P., Röder, Achim, & Hill, J. (2003). Coupling spectral unmixing and trend analysis for monitoring of long-term vegetation dynamics in Mediterranean rangelands. *Remote Sensing of Environment*, 87, 183–197.

- Howard, S. M., Ohlen, D. O., McKinley, R. A., Zhu, Z., & Kitchen, J. (2002). Historical fire severity mapping from Landsat data. Pecora 15/Land Satellite Information IV/ ISPRS Commission I Symposium. *Proceedings. American Society for Photogrammetry and Remote Sensing*.
- Huang, C., Goward, S. N., Masek, J. G., Thomas, N., Zhu, Z., & Vogelmann, J. E. (2010). An automated approach for reconstructing recent forest disturbance history using dense Landsat time series stacks. *Remote Sensing of Environment*, 114, 183–198.
- Irish, R. (2000). Landsat-7 automatic cloud cover assessment algorithms for multispectral, hyperspectral, and ultraspectral imagery. *The International Society for Optical Engineering*, 4049, 348–355.
- Irish, R. R., Barker, J. L., Goward, S. N., & Arvidson, T. (2006). Characterization of the Landsat-7 ETM+ Automated Cloud-Cover Assessment (ACCA) Algorithm. *Photogrammetric Engineering & Remote Sensing*, 72(10), 1179–1188.
- Jensen, J. R., Rutchey, K., Koch, M. S., & Narumalani (1995). Inland wetland change detection in the everglades water conservation area 2A using a time series of normalized remotely sensed data. *Photogrammetric Engineering and Remote Sensing*, 61(2), 199–209.
- Kennedy, R. E., Cohen, W. B., & Schroeder, T. A. (2007). Trajectory-based change detection for automated characterization of forest disturbance dynamics. *Remote Sensing of Environment*, 110, 370–386.
- Kennedy, R. E., Yang, Z., & Cohen, W. B. (2010). Detecting trends in forest disturbance and recovery using yearly Landsat time series: 1. *LandTrendr - Temporal segmentation algorithms*. *Remote Sensing of Environment*, 114(12), 2897–2910.
- Masek, J. G., Huang, C., Wolfe, R., Cohen, W., Hall, F., Kutler, J., et al. (2008). North American forest disturbance mapped from decadal Landsat record. *Remote Sensing of Environment*, 112, 2914–2926.
- Masek, J. G., Vermote, E. F., Saleous, N., Wolfe, R., Hall, E. F., Huemmrich, F., et al. (2006). A Landsat surface reflectance data set for North America, 1990–2000. *Geoscience and Remote Sensing Letters*, 3, 68–72.
- O'Leary, D. P. (1990). Robust regression computation using iteratively reweighted least squares. *Society for Industrial and Applied Mathematics*, 11(3), 466–480.
- Rayner, J. N. (1971). *An introduction to spectral analysis*. London: Pion Ltd. 174.
- Roy, D. P., Ju, J., Lewis, P., Schaaf, C., Gao, F., Hansen, M., & Lindquist, E. (2008). Multi-temporal MODIS-Landsat data fusion for relative radiometric normalization gap filling, and prediction of Landsat data. *Remote Sensing of Environment*, 112(3), 3112–3130.
- Seto, K. C., Woodcock, C. E., Song, C., Huang, X., Lu, J., & Kaufmann, R. K. (2002). Monitoring land-use change in the Pearl River Delta using Landsat TM. *International Journal of Remote Sensing*, 23(10), 1985–2004.
- Simpson, J. J., & Stitt, J. R. (1998). A procedure for the detection and removal of cloud shadow from AVHRR data over land. *Geoscience and Remote Sensing*, 36(3), 880–890.
- Street, J. O., Carroll, R. J., & Ruppert, D. (1988). A note on computing robust regression estimates via iteratively reweighted least squares. *American Statistical Association*, 42(2), 152–154.
- Takao, G. (2003). Indices from snow-covered Landsat imagery for boreal forest change detection. *Journal of the Japan Society of Photogrammetry and Remote Sensing*, 42(6), 52–66.
- Tucker, C. J. (1979). Red and photographic infrared linear combinations for monitoring vegetation. *Remote Sensing of Environments*, 8, 127–150.
- Vermote, E. F., El Saleous, N., Justice, C. O., Kaufman, Y. J., Privette, J. L., et al. (1997). Atmospheric correction of visible to middle-infrared EOS-MODIS data over land surfaces: Background, operational algorithm, and validation. *Journal of Geophysical Research*, 102, 17131–17141.
- Vogelmann, J. E., Tolk, B., & Zhu, Z. (2009). Monitoring forest changes in the southwestern United States using multitemporal Landsat data. *Remote Sensing of Environment*, 113, 1739–1748.
- Woodcock, C. E., Macomber, S. A., Pax-Lenney, M., & Cohen, W. B. (2001). Large area monitoring of temperate forest change using Landsat data: Generalization across sensors, time and space. *Remote Sensing of Environment*, 78(1–2), 194–203.
- Zhu, Z., & Woodcock, C. E. (2012). Object-based cloud and cloud shadow detection in Landsat imagery. *Remote Sensing of Environment*, 118(15), 83–94.
- Zhu, Z., Woodcock, C. E., & Olofsson, P., Automated cloud and cloud shadow screening based on multi-temporal Landsat imagery. *In preparation*.